Computational Mechanics (2022) 69:1131–1146
https://doi.org/10.1007/s00466-021-02133-y

ORIGINAL PAPER

Modeling elasticity of cubic crystals using a novel nonlocal lattice particle method

Hailong Chen[1] · Changyu Meng[2] · Yongming Liu[2]

Received: 11 October 2021 / Accepted: 29 November 2021 / Published online: 22 January 2022

Abstract
A novel nonlocal lattice particle method for modeling elastic deformation of cubic crystals was proposed and verified in this paper. Different from all other numerical models, the lattice particle method decomposes the grain domain into regularly packed discrete material particles according to the internal crystal lattice. Two most common Bravais cubic lattices, i.e., the body-centered cubic lattice and the face-center cubic lattice, were studied in this work. Model parameters were derived in terms of the three elastic material constants based on energy equivalency and theory of hyper-elasticity. Different from coordinates transformation used in the classical continuum mechanics theory, rotation of the discretization lattice is employed to equivalently represent the material anisotropy while capturing the underlying microstructure in the proposed model. The validity and prediction accuracy of the proposed model were established by comparing the predicted directional Young's modulus and the resolved shear stress of different slip systems against analytical solutions.

Keywords Crystal elasticity · Cubic crystals · Lattice particle method · Lattice rotation · Resolved shear stress

1 Introduction

Crystalline materials are commonly used in engineering applications crossing different length scales, such as large-scale metal alloys and ceramics in civil systems and micro-components for micro-electro-mechanical systems (MEMS) [1]. The physical properties of crystalline materials are uniquely determined by the microstructural features of internal grains, including the morphology, size distribution, anisotropy and crystallographic orientation [2]. The behavior of crystalline materials at the mesoscale can be studied by both experiments [3, 4] and computational models [5, 6]. In terms of computational modeling, extensive research has been performed to develop computational methods for the modeling and simulation of failure of polycrystalline microstructures across multiple length scales. These includes methods at the microscale, such as molecular dynamics [7, 8], methods at the mesoscale, such as cohesive zone models [9–11], extended finite elements [12, 13], phase field models [14–16], percolation model [17, 18] and peridynamics [19–21], and methods that couple these two length scales, such as quasi-continuum method [22, 23] and concurrent atomic-continuum approach [24, 25]. The microscale models focus on investigating the grain boundary effects and can only handle small polycrystal systems due to prohibitive computational cost. On the other hand, the mesoscale models can handle large polycrystal systems but at the sacrifice of lower length scale information. The multiscale methods aim to improve the computational efficiency while being able to consider the lower length scale details at locations of interest.

For models at the mesoscale, the conventional way of modeling anisotropic materials has been used, i.e., material anisotropy is represented using anisotropic constitutive law while the internal crystal lattice that results in this material anisotropy is neglected [26]. For the case of cubic crystals, because of the cubic symmetry of its underlying lattice, three independent material constants are used to fully characterize the elastic behavior under the principal coordinates system. For an arbitrarily oriented grain in space, coordinates transformation is used to transform the material stiffness tensor from the principal coordinates system to the global coordinates system. No information regarding the cubic symmetry of the internal crystal lattice that results in the cubic

✉ Hailong Chen
hailong.chen@uky.edu

[1] Department of Mechanical Engineering, University of Kentucky, Lexington, KY 40506, USA

[2] School for Engineering of Matter, Transport and Energy, Arizona State University, Tempe, AZ 85281, USA

material stiffness tensor is directly modeled. This is understandable since continuum-level models are developed based on the idea of homogenization. All microstructural features are homogenized out or neglected in the continuum-level models. However, for mesoscale or grain scale modeling and simulation, the internal crystal lattice plays important role in determining its mechanical behavior, such as in determining the cleavage planes [27] and slip planes [28]. Therefore, being able to represent the lattice structure in the geometric model is beneficial to the study of the mechanical behavior of crystalline materials at the mesoscale.

In this paper, we propose a novel nonlocal meshfree model based on a recently developed lattice particle method (LPM) for modeling the elastic behavior of single cubic crystals at the mesoscale. Although demonstrated using cubic crystals, the proposed methodology can be applied to model other types of crystals such as the hexagonal close packed crystals. Compared to other computational models based on the classical continuum mechanics theory, the novelties of the proposed model lie in at least the following two aspects: First, LPM reformulates the classical continuum mechanics theory using discretized integro-differential equations by decomposing a material domain as an assemblage of regularly packed material particles according to Bravais lattices. The interactions between material particles are completely nonlocal that a material particle interacts with neighboring material particles up to certain distance and the interaction between two material particles depends on all the neighbors of these two material particles. This better avoid the spatial discontinuity related stress singularity issue in the classical continuum mechanics theory [29]; Second, for modeling crystalline materials, in addition to the anisotropic constitutive law, the internal lattice that results in this anisotropy in material property is explicitly captured in the geometry model. This would greatly facilitate the modeling and simulation process where information regarding specific lattice plane is useful and needed.

The remainder of this paper is organized as follows. In Sect. 2, a brief review of the general formulation of LPM for linear elastic solids is given. A realization of the general formulation for cubic crystals using body-centered cubic (bcc) lattice and face-centered cubic (fcc) lattice is presented in Sect. 3. Rotation of the discretization lattice to accurately represent the crystallographic orientation hence the material anisotropy of a crystal is also discussed. In Sect. 4, two benchmark examples regarding the directional Young's modulus and the resolved shear stress of different slip systems are studied to assess the performance of the proposed model. Discussions and conclusions are drawn in Sect. 5.

2 Linear elasticity using nonlocal lattice particle method: a review

Lattice particle method (LPM) is a nonlocal meshfree reformulation of the classical continuum mechanics theory by replacing the governing partial differential equations with discretized integro-differential equations. By virtue of this reformulation, LPM doesn't have any numerical issues, such as stress singularity, resulted from the existence of spatial discontinuities in the solution domain. Therefore, LPM offers some unique benefits in modeling and simulating material failure behavior [29]. A brief review of the general formulation of LPM for linear elastic solids is presented in this section. Detailed formulations can be found in Refs. [30–32].

In LPM, the material domain is discretized into regularly packed material particles according to a given Bravais lattice. Discrete material particles interact with neighboring material particles up to certain distance via bonds, and unit cells are identified for neighboring material particles of the same distance. In LPM, the total potential energy at a material particle is the summation of all the energies of the unit cells associated with the material particle as

$$U_{particle} = \sum_{I=1}^{n_c} U_{cell\_I}, \tag{1}$$

where n_c is the number of unit cells associated with a material particle. The potential energy of a unit cell in LPM is different from that in the classical lattice spring model [33]. In LPM, both local pairwise and nonlocal multi-body potentials are employed to describe the potential energy, which can be written as

$$U_{cell\_I} = U_{local\_I} + U_{nonlocal\_I} = \sum_{\beta=1}^{n_c^{(I)}} \frac{1}{2}\left(\frac{1}{2}k^{(\beta)}\left(\delta l^{(\beta)}\right)^2\right) + \frac{1}{2}\left(\sum_{\beta=1}^{n_c^{(I)}} T^{(\beta)}\frac{\delta l^{(\beta)}}{2}\right)\left(\sum_{\beta=1}^{n_c^{(I)}} \frac{\delta l^{(\beta)}}{2}\right), \tag{2}$$

where U_{local_I} is the total pair-wise potential energy of individual bonds associated with the unit cell I, $U_{nonlocal\_I}$ is the nonlocal multi-body potential energy related to the collective behavior of all bonds associated with the unit cell I, k and T are the local and nonlocal stiffness parameters for each bond β,respectively, $n_c^{(I)}$ is the total number of neighboring material particles associated with unit cell I, δl is the bond elongation. It is noteworthy that a factor of $1/2$ is used to account the equal contribution of the energy of a bond to the two material particles in the local component and only half of the bond elongation is used in the nonlocal component.

For infinitesimal strain problems, the bond elongation δl can be related to the strain tensor ε_{ij} for a material particle [34] as

$$e = \frac{\delta l}{L} = N_i N_j \varepsilon_{ij}, \tag{3}$$

where $\boldsymbol{N}$ is the unit vector in the bond direction and L is the initial bond length. Plugging Eq. (3) into Eq. (2), the total potential energy of a unit cell can be rewritten in terms of the components of a strain tensor as

$$\begin{aligned} U_{cell\_I} = & \frac{1}{4}\sum_{\beta=1}^{n_c^{(I)}}\left(k^{(\beta)}\left(L^{(\beta)}\right)^2 N_i^{(\beta)} N_j^{(\beta)} N_k^{(\beta)} N_l^{(\beta)} \varepsilon_{ij}\varepsilon_{kl}\right) \\ & + \frac{1}{8}\sum_{\beta=1}^{n_c^{(I)}}\left(T^{(\beta)} L^{(\beta)} N_i^{(\beta)} N_j^{(\beta)} \varepsilon_{ij}\right)\sum_{\beta=1}^{n_c^{(I)}}\left(L^{(\beta)} N_k^{(\beta)} N_l^{(\beta)} \varepsilon_{kl}\right), \end{aligned} \tag{4}$$

Therefore, the total potential energy of a material particle can be expressed as

$$\begin{aligned} & U_{particle} \\ & = \sum_{I=1}^{n_c}\left(\frac{1}{4}\sum_{\beta=1}^{n_c^{(I)}} k^{(\beta)}\left(L^{(\beta)}\right)^2 N_i^{(\beta)} N_j^{(\beta)} N_k^{(\beta)} N_l^{(\beta)} \varepsilon_{ij}\varepsilon_{kl}\right. \\ & \left. + \frac{1}{8}\sum_{\beta=1}^{n_c^{(I)}} T^{(\beta)} L^{(\beta)} N_i^{(\beta)} N_j^{(\beta)} \varepsilon_{ij} \sum_{\beta=1}^{n_c^{(I)}} L^{(\beta)} N_k^{(\beta)} N_l^{(\beta)} \varepsilon_{kl}\right). \end{aligned} \tag{5}$$

By equivalating the potential energy of an LPM material particle to that of a continuum counterpart, the material stiffness tensor can be obtained by the theory of hyper-elasticity as

$$\begin{aligned} C_{ijkl} = & \frac{1}{V}\frac{\partial^2 U_{particle}}{\partial\varepsilon_{ij}\partial\varepsilon_{kl}} \\ = & \frac{1}{V}\sum_{I=1}^{n_c}\left(\frac{1}{2}\sum_{\beta=1}^{n_c^{(I)}} k^{(\beta)}\left(L^{(\beta)}\right)^2 N_i^{(\beta)} N_j^{(\beta)} N_k^{(\beta)} N_l^{(\beta)}\right. \\ & \left. + \frac{1}{4}\sum_{\beta=1}^{n_c^{(I)}} T^{(\beta)} L^{(\beta)} N_k^{(\beta)} N_l^{(\beta)} \sum_{\beta=1}^{n_c^{(I)}} L^{(\beta)} N_i^{(\beta)} N_j^{(\beta)}\right), \end{aligned} \tag{6}$$

where V is the volume of a LPM material particle, which is usually the same as the volume of the unit cell for the first nearest neighbors. For homogeneous Hookean materials, the model parameters can be solved by matching the derived material stiffness tensor in Eq. (6) with the one from the continuum mechanics expressed in terms of materials constants, such as Young's modulus and Poisson's ratio for isotropic materials.

Assuming the model parameters are known and given the potential energy of each material particle, the interaction force between material particles can be calculated by differentiating the potential energy with respect to the length change δl of the bond as

$$\boldsymbol{F}^{(\alpha\beta)} = -\frac{\partial\left(U_{particle}^{(\alpha)} + U_{particle}^{(\beta)}\right)}{\partial\left(\delta l^{(\alpha\beta)}\right)}\boldsymbol{n}^{(\alpha\beta)}, \tag{7}$$

where $\boldsymbol{n}^{(\alpha\beta)}$ is the unit vector between particle α and its neighboring material particle β. Carrying out the differentiation, the force magnitude can be found as

$$\begin{aligned} F^{(\alpha\beta)} = & \frac{\partial U_{particle}^{(\alpha)}}{\partial\left(\delta l^{(\alpha\beta)}\right)} + \frac{\partial U_{particle}^{(\beta)}}{\partial\left(\delta l^{(\alpha\beta)}\right)} = k^{(\alpha\beta)}\delta l^{(\alpha\beta)} \\ & + \frac{1}{8}\left(T^{(\alpha)}\sum_{\gamma=1}^{n_c^{(\beta)}}\delta l^{(\alpha\gamma)} + \sum_{\gamma=1}^{n_c^{(\beta)}} T^{(\gamma)}\delta l^{(\alpha\gamma)}\right. \\ & \left. + T^{(\beta)}\sum_{\gamma=1}^{n_c^{(\alpha)}}\delta l^{(\beta\gamma)} + \sum_{\gamma=1}^{n_c^{(\alpha)}} T^{(\gamma)}\delta l^{(\beta\gamma)}\right), \end{aligned} \tag{8}$$

where $n_c^{(\beta)}$ is for material particle α's unit cell that includes material particle β and $n_c^{(\alpha)}$ is for material particle β's unit cell that includes material particle α. As can be seen from Eq. (8), the force between two interacting material particles is completely nonlocal, namely, the interaction depends on not only the bond connecting these two material particles but also the bonds connecting these two material particles with their neighbors that shares the same unit cells as these two material particles. The total internal force for a material particle is the summation of the forces from all its neighboring material particles as

$$\boldsymbol{F}_{int} = \sum_{\beta=1}^{\sum_{I=1} n_c n_c^{(I)}} \boldsymbol{F}^{(\beta)}. \tag{9}$$

Finally, the Equations of Motion for a material particle in LPM has the following form

$$m\ddot{\boldsymbol{u}} = \boldsymbol{F}_{int} + \boldsymbol{b}, \tag{10}$$

with m being the mass of a material particle, $\boldsymbol{u}$ is the displacement vector, and $\boldsymbol{b}$ is the body force. For dynamic problems, Eq. (10) can be solved using standard explicit time integration schemes, such as Verlet integration [29]. For static or quasi-static problems, the implicit solution scheme based on energy minimization can be used [30, 35].

Continuum-like measures such as strain and stress tensors can be constructed at each material particle based on the bond elongation and force using the least squares technique [34]. The second Piola–Kirchhoff (PK2) stress tensor at a material particle can be approximated from the bond force as

$$S_{ij}^{PK2} = \frac{1}{V}\sum_{I=1}^{n_c}\sum_{\beta=1}^{n_c^{(I)}} L^{(\beta)} F^{(\beta)} N_i^{(\beta)} N_j^{(\beta)}. \tag{11}$$

where $F^{(\beta)}$ is the force magnitude of neighbor β.

For infinitesimal strain problems, the PK2 stress is approximately the same as the Cauchy stress σ_{ij}.

So far, the general formulation of LPM for linear elastic solids has been briefly reviewed. The number of LPM parameters needed for full description of material elastic behavior is dependent on the number of independent elastic materials constants, i.e., material symmetry. In the following Sect. 3, this formulation will be applied to develop a LPM cubic crystal elasticity model. Explicit expression of the model parameters in terms of the three elastic material constants will be derived. The simplified form of the interaction force for a specific lattice will also be given.

3 Cubic linear elasticity using nonlocal lattice particle method

To model the linear elastic behavior of cubic crystals, three independent elastic material constants are needed, namely, the C_{11}, C_{12} and C_{44}. The Voigt notation of the material stiffness tensor for cubic crystals in the classical continuum mechanics theory can be written as

$$\mathbf{C}_{cm} = \begin{bmatrix} C_{11} & C_{12} & C_{12} & 0 & 0 & 0 \\ C_{12} & C_{11} & C_{12} & 0 & 0 & 0 \\ C_{12} & C_{12} & C_{11} & 0 & 0 & 0 \\ 0 & 0 & 0 & C_{44} & 0 & 0 \\ 0 & 0 & 0 & 0 & C_{44} & 0 \\ 0 & 0 & 0 & 0 & 0 & C_{44} \end{bmatrix}. \tag{12}$$

In LPM, three independent model parameters are needed in order to fully describe the elastic behavior of cubic crystals. Therefore, based on the cubic symmetry and the structure of bcc and fcc lattices, the minimum required neighboring interacting material particles are the first and the second nearest neighbors. Furthermore, bonds connecting a material particle with the same types of neighbors, i.e., either the first or the second nearest neighbors, have the same local parameter k and nonlocal parameter T. But these two parameters for the first and the second nearest neighbors are different in general, e.g., the local parameter k for the first nearest neighbors is different from that for the second nearest neighbors. However, to match the number of independent elastic material constants from the continuum mechanics theory, the nonlocal parameter T of the first nearest neighbors is assumed to be identical to that of the second nearest neighbors. As a result, there are three independent model parameters in LPM for cubic crystals, i.e., $k^{(1)}$, $k^{(2)}$, and T, and the minimum neighbors need to be considered are the first and the second nearest neighbors. As will be seen later in this section, these three model parameters are uniquely determined in terms of the three elastic material constants.

Therefore, for cubic crystals, the potential energy of an LPM material particle has the following simplified form as

$$\begin{aligned} U_{particle} = {} & \frac{1}{2}\sum_{\beta=1}^{n_c^{(1)}} \frac{1}{2}k^{(1)}\left(\delta l^{(\beta)}\right)^2 + \frac{1}{2}T\left(\sum_{\beta=1}^{n_c^{(1)}} \frac{\delta l^{(\beta)}}{2}\right)^2 \\ & + \frac{1}{2}\sum_{\beta=1}^{n_c^{(2)}} \frac{1}{2}k^{(2)}\left(\delta l^{(\beta)}\right)^2 + \frac{1}{2}T\left(\sum_{\beta=1}^{n_c^{(2)}} \frac{\delta l^{(\beta)}}{2}\right)^2. \end{aligned} \tag{13}$$

In terms of the components of strain tensor, the above potential energy can be rewritten as

$$\begin{aligned} U_{particle} = {} & \frac{1}{4}k^{(1)}\left(L^{(1)}\right)^2 \sum_{\beta=1}^{n_c^{(1)}}\left(N_i^{(\beta)}N_j^{(\beta)}N_k^{(\beta)}N_l^{(\beta)}\varepsilon_{ij}\varepsilon_{kl}\right) \\ & + \frac{1}{8}T\left(L^{(1)}\sum_{\beta=1}^{n_c^{(1)}} N_i^{(\beta)}N_j^{(\beta)}\varepsilon_{ij}\right)\left(L^{(1)}\sum_{\beta=1}^{n_c^{(1)}} N_k^{(\beta)}N_l^{(\beta)}\varepsilon_{kl}\right) \\ & + \frac{1}{4}k^{(2)}\left(L^{(2)}\right)^2 \sum_{\beta=1}^{n_c^{(2)}}\left(N_i^{(\beta)}N_j^{(\beta)}N_k^{(\beta)}N_l^{(\beta)}\varepsilon_{ij}\varepsilon_{kl}\right) \\ & + \frac{1}{8}T\left(L^{(2)}\sum_{\beta=1}^{n_c^{(2)}} N_i^{(\beta)}N_j^{(\beta)}\varepsilon_{ij}\right)\left(L^{(2)}\sum_{\beta=1}^{n_c^{(2)}} N_k^{(\beta)}N_l^{(\beta)}\varepsilon_{kl}\right). \end{aligned} \tag{14}$$

The material stiffness tensor can be determined by the theory of hyper-elasticity as

$$\begin{aligned} \mathbb{C}_{ijkl} = {} & \frac{1}{V}\frac{\partial^2 U_{particle}}{\partial\varepsilon_{ij}\partial\varepsilon_{kl}} \\ = {} & \frac{1}{2V}\left(k^{(1)}\left(L^{(1)}\right)^2 \sum_{\beta=1}^{n_c^{(1)}}\left(N_i^{(\beta)}N_j^{(\beta)}N_k^{(\beta)}N_l^{(\beta)}\right)\right. \\ & + \frac{1}{2T}\left(L^{(1)}\right)^2 \left(\sum_{\beta=1}^{n_c^{(1)}} N_i^{(\beta)}N_j^{(\beta)}\right)\left(\sum_{\beta=1}^{n_c^{(1)}} N_k^{(\beta)}N_l^{(\beta)}\right) \\ & \left. + k^{(2)}\left(L^{(2)}\right)^2 \sum_{\beta=1}^{n_c^{(2)}}\left(N_i^{(\beta)}N_j^{(\beta)}N_k^{(\beta)}N_l^{(\beta)}\right)\right. \end{aligned}$$

$$+\frac{1}{2T}\left(L^{(2)}\right)^2\left(\sum_{\beta=1}^{n_c^{(2)}} N_i^{(\beta)} N_j^{(\beta)}\right)\left(\sum_{b_2=1}^{n_c^{(2)}} N_k^{(\beta)} N_l^{(\beta)}\right)\Bigg). \tag{15}$$

The magnitude of the bond interaction force can also be simplified as

$$F^{(\alpha\beta)} = \begin{cases} k^{(1)}\delta l^{(\alpha\beta)} + \frac{T}{4}\left(\sum_{\gamma=1}^{n_c^{(1)}} \delta l^{(\alpha\gamma)} + \sum_{\gamma=1}^{n_c^{(1)}} \delta l^{(\beta\gamma)}\right), & \text{if } \beta \text{ is the 1st neighbor of } \alpha \\ k^{(2)}\delta l^{(\alpha\beta)} + \frac{T}{4}\left(\sum_{\gamma=1}^{n_c^{(2)}} \delta l^{(\alpha\gamma)} + \sum_{\gamma=1}^{n_c^{(2)}} \delta l^{(\beta\gamma)}\right), & \text{if } \beta \text{ is the 2nd neighbor of } \alpha \end{cases}. \tag{16}$$

As a result of the nonlocality of the interaction between material particles, LPM doesn't possess any limitation on the range of Poisson's ratio. LPM can be applied to model materials with Poisson's ration in the range of -1.0 to $+0.5$ [30, 32]. In the following subsections, the explicit forms of the three model parameters will be derived in terms of the three elastic material constants for two cubic Bravais lattices, namely, the body-centered cubic (bcc) and the face-centered cubic (fcc).

3.1 Body-centered cubic lattice

For bcc lattice, there are total of 14 interacting neighbors for each material particle, eight of which are the first nearest neighbors and the rest six are the second nearest neighbors. The unit cells for the two types of neighbors are shown in Fig. 1. The corresponding 14 bond unit vectors are given in Table 1. The R is half the distance between a material particle with its first nearest neighbors.

Plugging the bond unit vectors given in Table 1 into Eq. (15), the material stiffness tensor in Voigt form using bcc lattice can be found as

$$\mathbf{C}_{bcc} = \begin{bmatrix} \frac{\sqrt{3}k_1}{6R} + \frac{\sqrt{3}k_2}{2R} + \frac{7\sqrt{3}T}{6R} & \frac{\sqrt{3}k_1}{6R} + \frac{7\sqrt{3}T}{6R} & \frac{\sqrt{3}k_1}{6R} + \frac{7\sqrt{3}T}{6R} & & \\ \frac{\sqrt{3}k_1}{6R} + \frac{7\sqrt{3}T}{6R} & \frac{\sqrt{3}k_1}{6R} + \frac{\sqrt{3}k_2}{2R} + \frac{7\sqrt{3}T}{6R} & \frac{\sqrt{3}k_1}{6R} + \frac{7\sqrt{3}T}{6R} & [0]_{3x3} & \\ \frac{\sqrt{3}k_1}{6R} + \frac{7\sqrt{3}T}{6R} & \frac{\sqrt{3}k_1}{6R} + \frac{7\sqrt{3}T}{6R} & \frac{\sqrt{3}k_1}{6R} + \frac{\sqrt{3}k_2}{2R} + \frac{7\sqrt{3}T}{6R} & & \\ & [0]_{3x3} & & \frac{\sqrt{3}k_1}{6R} & 0 & 0 \\ & & & 0 & \frac{\sqrt{3}k_1}{6R} & 0 \\ & & & 0 & 0 & \frac{\sqrt{3}k_1}{6R} \end{bmatrix}. \tag{17}$$

Comparing the material stiffness matrices in Eq. (17) and Eq. (12), the model parameters for bcc lattice considering the first and the second nearest neighbors can be uniquely determined as

$$\begin{Bmatrix} k^{(1)} \\ k^{(2)} \\ T \end{Bmatrix} = R \begin{bmatrix} 0 & 0 & 2\sqrt{3} \\ \frac{2\sqrt{3}}{3} & -\frac{2\sqrt{3}}{3} & 0 \\ 0 & \frac{2\sqrt{3}}{7} & -\frac{2\sqrt{3}}{7} \end{bmatrix} \begin{Bmatrix} C_{11} \\ C_{12} \\ C_{44} \end{Bmatrix}. \tag{18}$$

3.2 Face-centered cubic lattice

For fcc lattice, there are total of 18 interacting neighbors for each material particle, 12 of which are the first nearest neighbors and the rest six are the second nearest neighbors. The unit cells for these two types of neighbors are shown in Fig. 2. The corresponding 18 bond unit vectors are given in Table 2.

Plugging the bond unit vectors in Table 2 into Eq. (15), the material stiffness tensor in Voigt form using fcc lattice can be found as

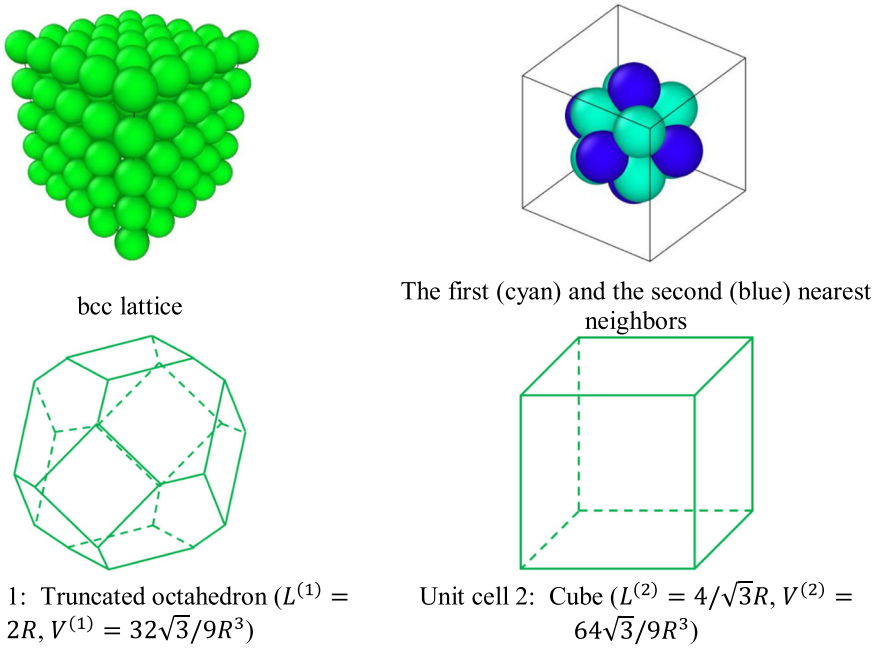

Fig. 1 The bcc lattice, neighbors and unit cells

$$\mathbf{C}_{fcc} = \begin{bmatrix} \frac{\sqrt{2}k_1}{2R} + \frac{\sqrt{2}k_2}{R} + \frac{3\sqrt{2}T}{R} & \frac{\sqrt{2}k_1}{4R} + \frac{3\sqrt{2}T}{R} & \frac{\sqrt{2}k_1}{4R} + \frac{3\sqrt{2}T}{R} & [0]_{3x3} \\ \frac{\sqrt{2}k_1}{4R} + \frac{3\sqrt{2}T}{R} & \frac{\sqrt{2}k_1}{2R} + \frac{\sqrt{2}k_2}{R} + \frac{3\sqrt{2}T}{R} & \frac{\sqrt{2}k_1}{4R} + \frac{3\sqrt{2}T}{R} & \\ \frac{\sqrt{2}k_1}{4R} + \frac{3\sqrt{2}T}{R} & \frac{\sqrt{2}k_1}{4R} + \frac{3\sqrt{2}T}{R} & \frac{\sqrt{2}k_1}{2R} + \frac{\sqrt{2}k_2}{R} + \frac{3\sqrt{2}T}{R} & \\ [0]_{3x3} & & & \begin{matrix} \frac{\sqrt{2}k_1}{4R} & 0 & 0 \\ 0 & \frac{\sqrt{2}k_1}{4R} & 0 \\ 0 & 0 & \frac{\sqrt{2}k_1}{4R} \end{matrix} \end{bmatrix}. \tag{19}$$

Comparing the material stiffness matrices in Eqs. (19) and (12), the model parameters for fcc lattice considering the first and the second nearest neighbors can be uniquely determined as

$$\begin{Bmatrix} k^{(1)} \\ k^{(2)} \\ T \end{Bmatrix} = R \begin{bmatrix} 0 & 0 & 2\sqrt{2} \\ \frac{\sqrt{2}}{2} & -\frac{\sqrt{2}}{2} & -\frac{\sqrt{2}}{2} \\ 0 & \frac{\sqrt{2}}{6} & -\frac{\sqrt{2}}{6} \end{bmatrix} \begin{Bmatrix} C_{11} \\ C_{12} \\ C_{44} \end{Bmatrix} \tag{20}$$

As can be seen from the second equality of Eq. (20), it is possible that the local parameter $k^{(2)}$ for the second nearest neighbors of the fcc lattice becomes negative when $C_{11} < C_{12} + C_{44}$, i.e., when the anisotropy factor $2C_{44}/(C_{11} - C_{12}) > 2$ for fcc crystals such as Copper. However, the bond forces whose calculation depend on this parameter could be still positive due to the nonlocal contributions from all the neighbors, as can be seen in Eq. (16). Nonetheless, the rest model parameters for both lattices are guaranteed to be positive for all cubic crystals (see Eqs. (18) and (20)). This non-positiveness of the local parameter $k^{(2)}$ for the fcc lattice will not affect the numerical performance of the proposed LPM model using fcc lattice, as will be demonstrated in the numerical study section.

Table 1 The bond unit vectors of all neighbors for bcc lattice

The first nearest neighbors		
$\left(\frac{1}{\sqrt{3}}, \frac{1}{\sqrt{3}}, -\frac{1}{\sqrt{3}}\right)$	$\left(-\frac{1}{\sqrt{3}}, \frac{1}{\sqrt{3}}, -\frac{1}{\sqrt{3}}\right)$	$\left(-\frac{1}{\sqrt{3}}, -\frac{1}{\sqrt{3}}, -\frac{1}{\sqrt{3}}\right)$
$\left(\frac{1}{\sqrt{3}}, -\frac{1}{\sqrt{3}}, -\frac{1}{\sqrt{3}}\right)$	$\left(\frac{1}{\sqrt{3}}, -\frac{1}{\sqrt{3}}, \frac{1}{\sqrt{3}}\right)$	$\left(-\frac{1}{\sqrt{3}}, \frac{1}{\sqrt{3}}, \frac{1}{\sqrt{3}}\right)$
$\left(-\frac{1}{\sqrt{3}}, -\frac{1}{\sqrt{3}}, \frac{1}{\sqrt{3}}\right)$	$\left(\frac{1}{\sqrt{3}}, \frac{1}{\sqrt{3}}, \frac{1}{\sqrt{3}}\right)$	
The second nearest neighbors		
(1, 0, 0)	(0, 1, 0)	(−1, 0, 0)
(0, −1, 0)	(0, 0, 1)	(0, 0, −1)

So far, the LPM model parameters have been derived in terms of the elastic material constants for cubic crystals for both bcc and fcc lattices. It is noteworthy that the derivation was developed under the crystal coordinates system or the principal coordinates system. To model cubic crystal arbitrarily oriented in the sample coordinates system or the global coordinates system, the crystallographic orientation must be

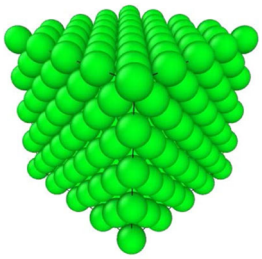

fcc lattice

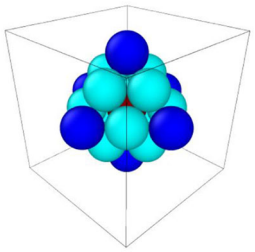

The first (cyan) and the second (blue) nearest neighbors

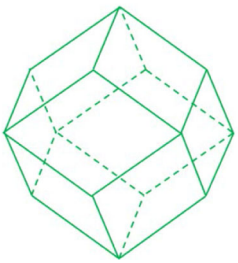

Unit cell 1: Rhombic dodecahedron ($L^{(1)} = 2R$, $V^{(1)} = 4\sqrt{2}R^3$)

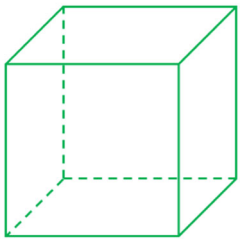

Unit cell 2: Cube ($L^{(2)} = 2\sqrt{2}R$, $V^{(2)} = 16\sqrt{2}R^3$)

Fig. 2 The fcc lattice, neighbors and unit cells

Table 2 The bond unit vectors of all neighbors for fcc lattice

The first nearest neighbors		
$\left(\frac{1}{\sqrt{2}}, -\frac{1}{\sqrt{2}}, 0\right)$	$\left(\frac{1}{\sqrt{2}}, \frac{1}{\sqrt{2}}, 0\right)$	$\left(-\frac{1}{\sqrt{2}}, \frac{1}{\sqrt{2}}, 0\right)$
$\left(-\frac{1}{\sqrt{2}}, -\frac{1}{\sqrt{2}}, 0\right)$	$\left(0, \frac{1}{\sqrt{2}}, -\frac{1}{\sqrt{2}}\right)$	$\left(0, \frac{1}{\sqrt{2}}, \frac{1}{\sqrt{2}}\right)$
$\left(0, -\frac{1}{\sqrt{2}}, \frac{1}{\sqrt{2}}\right)$	$\left(0, -\frac{1}{\sqrt{2}}, -\frac{1}{\sqrt{2}}\right)$	$\left(\frac{1}{\sqrt{2}}, 0, -\frac{1}{\sqrt{2}}\right)$
$\left(\frac{1}{\sqrt{2}}, 0, \frac{1}{\sqrt{2}}\right)$	$\left(-\frac{1}{\sqrt{2}}, 0, \frac{1}{\sqrt{2}}\right)$	$\left(-\frac{1}{\sqrt{2}}, 0, -\frac{1}{\sqrt{2}}\right)$
The second nearest neighbors		
$(1, 0, 0)$	$(0, 1, 0)$	$(-1, 0, 0)$
$(0, -1, 0)$	$(0, 0, 1)$	$(0, 0, -1)$

accurately accounted for. In Sect. 3.3, rotation of the discretization lattice to accurately represent the crystallographic orientation in LPM will be discussed.

3.3 Crystallographic orientation representation using lattice rotation

In the case when the crystal coordinates system is different from the sample coordinates system, the transformation of axes is used in the classical continuum mechanics theory to account for the crystallographic orientation. Different from the transformation of axes, lattice rotation or axes rotation is employed to represent the crystallographic orientation in LPM. Since the real underlying lattice is used to discretize the material domain and the derived model parameters are orientation dependent, lattice rotation can explicitly represent the crystallographic orientation and offers great benefits in modeling of crystalline materials using LPM.

In crystallography and texture analysis, the so-called Euler angles with Bunge convention [36] are commonly used for describing the orientation of each crystal. LPM adopts the Bunge convention to capture the crystallographic orientation of a crystal. To that end, one can consider going from a sample coordinate system (X, Y, Z) to a rotated crystal coordinate system (x, y, z) using three subsequent rotations. The angles associated to those elementary rotations are usually denoted as φ_1, Φ, φ_2, respectively. The subsequent rotations can be expressed as follows:

$$(X, Y, Z) \overset{Z\ axis:\varphi_1}{\rightarrow} (u, v, Z) \overset{u\ axis:\Phi}{\rightarrow} (u, w, z) \overset{z\ axis:\varphi_2}{\rightarrow} (x, y, z). \tag{21}$$

These three rotations are counterclockwise positive. The asymmetric units are given by the intervals [36]:

$$\varphi_1 \in \left[0, 360^\circ\right), \Phi \in \left[0, 180^\circ\right), \varphi_2 \in \left[0, 360^\circ\right). \tag{22}$$

As a result of these three subsequent rotations, the overall rotation matrix is the product of the three rotation matrices corresponding to the three elementary rotations, which is given as

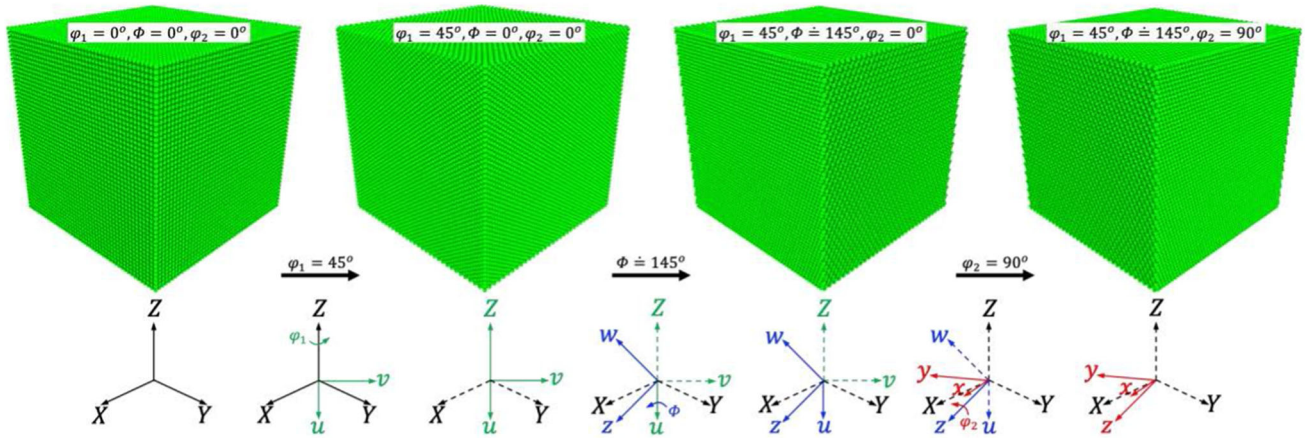

Fig. 3 Demonstration of lattice rotation to represent crystallographic orientation using bcc lattice (the crystal ⟨111⟩ direction aligns with the sample X-direction after a series of three rotations, the more accurate value for the second rotation is $\phi = 144.7356°$)

Table 3 The elastic constants of single cubic crystals [37] (GPa)

Cubic single crystals		C_{11}	C_{12}	C_{44}	Anisotropy factor $2C_{44}/(C_{11} - C_{12})$
bcc	α-Iron (α-Fe)	230	135	117	2.4632
	Niobium (Nb)	245	132	28.4	0.5027
fcc	Aluminum (Al)	108	62	28.3	1.2304
	Copper (Cu)	169	122	75.3	3.2043

$$R(\varphi_1, \Phi, \varphi_2) = \begin{bmatrix} cos\varphi_1 & sin\varphi_1 & 0 \\ -sin\varphi_1 & cos\varphi_1 & 0 \\ 0 & 0 & 1 \end{bmatrix} \begin{bmatrix} 1 & 0 & 0 \\ 0 & cos\Phi & sin\Phi \\ 0 & -sin\Phi & cos\Phi \end{bmatrix} \times \begin{bmatrix} cos\varphi_2 & sin\varphi_2 & 0 \\ -sin\varphi_2 & cos\varphi_2 & 0 \\ 0 & 0 & 1 \end{bmatrix}. \quad (23)$$

A demonstration of this lattice rotation process is presented in Fig. 3 using bcc lattice. Three subsequent rotations of $\varphi_1 = 45°$, $\Phi \doteq 145°$, and $\varphi_2 = 90°$ are applied to align the crystal ⟨1, 1, 1⟩ direction to the sample X-direction.

4 Numerical results

The proposed LPM model is numerically tested and verified in this section. Two benchmark examples concerning the elastic behavior of cubic crystals are studied. The first example applies the model to predict the directional Young's modulus of cubic crystals, while the second example verifies the predicted resolved shear stress (RSS) in each slip system of both bcc and fcc crystals. Four different cubic crystals are studied, and their elastic constants are tabulated in Table 3. Anisotropy factors are also calculated to indicate the degrees of elastic anisotropy of these four crystals. The closer the factor to value of 1, the less anisotropic or the more isotropic of the crystal elastic behavior. As can be seen from the calculated anisotropy factor, the Copper has the largest degree of elastic anisotropy, with value of 3.2043. As discussed in Sect. 3.2, the anisotropic factor of fcc crystals will determine the sign of the local parameter for the second nearest neighbor. Therefore, this local parameter for the case of modeling Copper is negative (see second equality of Eq. (20)).

All the numerical tests in this section are based on the same cubical crystal domain subjected to uniaxial tension loading in the Z-direction under the sample coordinates system, as shown in Fig. 4. The cube is constrained on the top surface and a uniform force of 100 N is applied on the bottom surface in the negative Z-direction. The whole top surface is fixed for the Z-displacement, and the surface center is fixed additionally both the X- and Y- displacements. Considering the dimensions of the cubical domain, the 100 N tensile force applied uniformly at the bottom surface is equivalent to a nominal tensile stress of 1 MPa on the bottom surface. For all cases studied in this section, there are about 200,000 material particles used in discretizing the cubical domain. The displacement of a surface under deformation is calculated as the average displacement of all the material particles on the surface. The implicit solution scheme based on energy minimization is used [30, 35].

4.1 Verification of directional Young's modulus

In this example, the accuracy of using the proposed LPM to model the elastic deformation of a single crystallite is examined. We compare the directional Young's modulus cal-

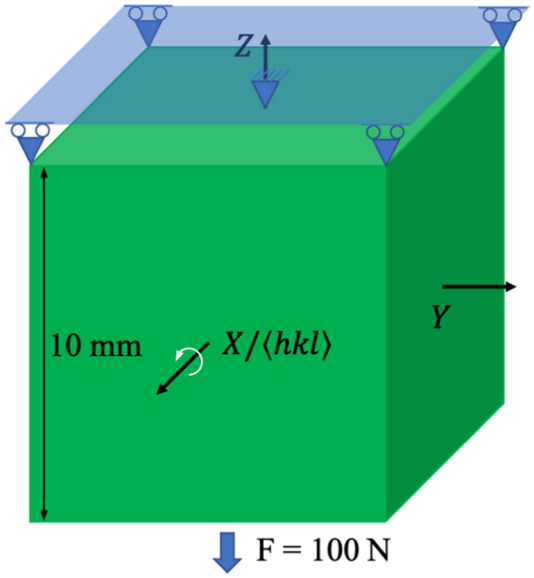

Fig. 4 Configuration of a cubical crystal domain

culated using LPM with the analytical solution from Ref. [38]. The analytical solution for the Young's modulus in any arbitrary direction $\langle hkl \rangle$ is given by

$$E^{Analytical}_{\langle hkl \rangle} = \frac{1}{S_{11} - 2\left(S_{11} - S_{12} - \frac{1}{2}S_{44}\right)\left(c_1^2c_2^2 + c_2^2c_3^2 + c_1^2c_3^2\right)}, \tag{24}$$

where S_{ij} are the components of the compliance matrix with $[\boldsymbol{S}] = \left[\boldsymbol{C}^{-1}\right]$; c_1, c_2 and c_3 are the direction cosine of the $\langle hkl \rangle$ direction with the $\langle 100 \rangle$, $\langle 010 \rangle$ and $\langle 001 \rangle$ crystal directions, respectively. The comparisons between the LPM predicted and analytical directional Young's moduli on the {100}, {110} and {111} crystal planes are shown in Figs. 5 and 6 for bcc and fcc crystals, respectively. To make sense of the three-dimensional variations of the Young's modulus, plots based on the analytical solution are also provided. The LPM predictions are generated by first rotating the $\langle 100 \rangle$, $\langle 110 \rangle$ and $\langle 111 \rangle$ crystal directions to align with the sample X-direction. The Bunge Euler angles are $(0°, 0°, 0°)$, $(315°, 0°, 0°)$ and $(45°, 145°, 90°)$, respectively. Simulations are then carried out for a series of in-plane angles from 0° to 90° at the increment of 15°. One additional angle of 35.3° for the case of Copper crystal is also used to calculate the maximum directional Young's modulus on the {110} planes. The directional Young's modulus is approximated using

$$E^{LPM}_{\langle hkl \rangle} = \frac{\sigma_{ZZ}}{\overline{u}_Z/L}, \tag{25}$$

where $\sigma_{ZZ} = 1$MPa is the equivalent applied stress, $L = 0.01$ m is the initial edge length of the cubical domain, and $\overline{u}_Z$ is the average Z-displacement on the bottom surface. The predicted values for the realizations of in-plane angles from 0° to 90° are then mapped to the interval of $[0, 360°)$ due to the symmetry of the cubic crystals.

As can be seen from the comparisons shown in Figss. 5 and 6, LPM can accurately reproduce the directional Young's modulus for both bcc and fcc single crystal. Both the anisotropy of the Young's modulus on the {100} and {110} crystal planes and the isotropy of the Young's modulus on the {111} crystal planes are accurately reproduced using LPM. For fcc crystals, the largest Young's modulus is in the crystal direction of $\langle 111 \rangle$, normal to the close packed planes. However, it is not general the case for bcc crystals. It should be noted that the negative local parameters $k^{(2)}$ for the case of Copper does not affect the performance of the model. As can be seen from the results in Fig. 6, LPM can accurately predict the directional Young's modulus on all the three crystal planes for Copper crystal, which is consistent with the LPM predictions for the other crystals.

4.2 Verification of resolved shear stress (RSS)

According to Schmid's law [39], crystal will begin to yield on a slip system when the shear stress on this slip system first reaches a critical value (critical resolved shear stress (CRSS)), independent of the tensile stress or any other normal stress on the crystal plane. In this example, we verify the predicted RSS using LPM for both lattices with the analytical value given by the Schmid law. The RSS τ_{RSS} by the Schmid's law can be calculated as

$$\tau_{RSS} = \sigma_{ZZ} cos\phi cos\lambda = \sigma_{ZZ} P, \tag{26}$$

where $cos\phi$ and $cos\lambda$ are the direction cosines of the slip direction vector and the normal vector of the slip plane with respective to the Z-axis of the sample coordinate system, respectively. The Schmid's factor $P = cos\phi cos\lambda$ can also be expressed in tensor form [40] as

$$P_{ij} = \frac{1}{2}\left(m_i n_j + m_j n_i\right), \tag{27}$$

where $\boldsymbol{m}$ is the slip direction vector and $\boldsymbol{n}$ is the corresponding normal vector of a slip system.

For infinitesimal strain problems, the RSS τ_{RSS} also can be expressed as

$$\tau_{RSS} = \sigma_{ij} P_{ij}, \tag{28}$$

Two different crystallographic orientations are considered, namely, $\left(0^0, 0^0, 0^0\right)$ and $\left(0^0, 45^0, 0^0\right)$ in terms of Bunge Euler angles. Under the same uniaxial loading along the Z-direction of the sample coordinate system, the resolved shear

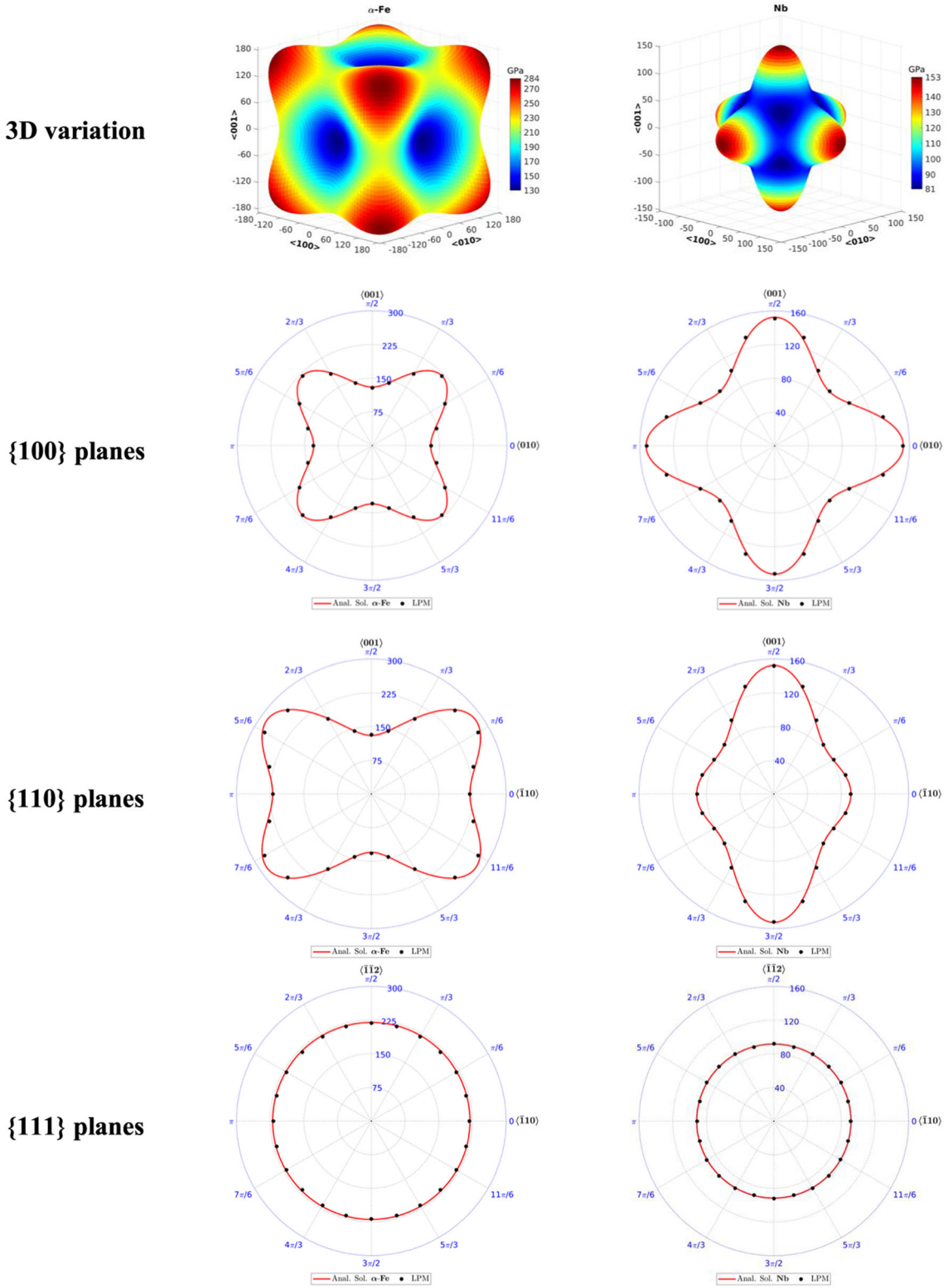

Fig. 5 Variation of Young's modulus of bcc α-Fe and Nb single crystals

stresses of all possible slip systems for both bcc and fcc lattices are calculated and compared. The predicted RSS by LPM, the RSS calculated using Schmid's law (Eq. (26)) and the relative error between them are tabulated in Table 4 and Table 5 for bcc and fcc lattices, respectively. The RSS in opposite directions have equal absolute values but opposite

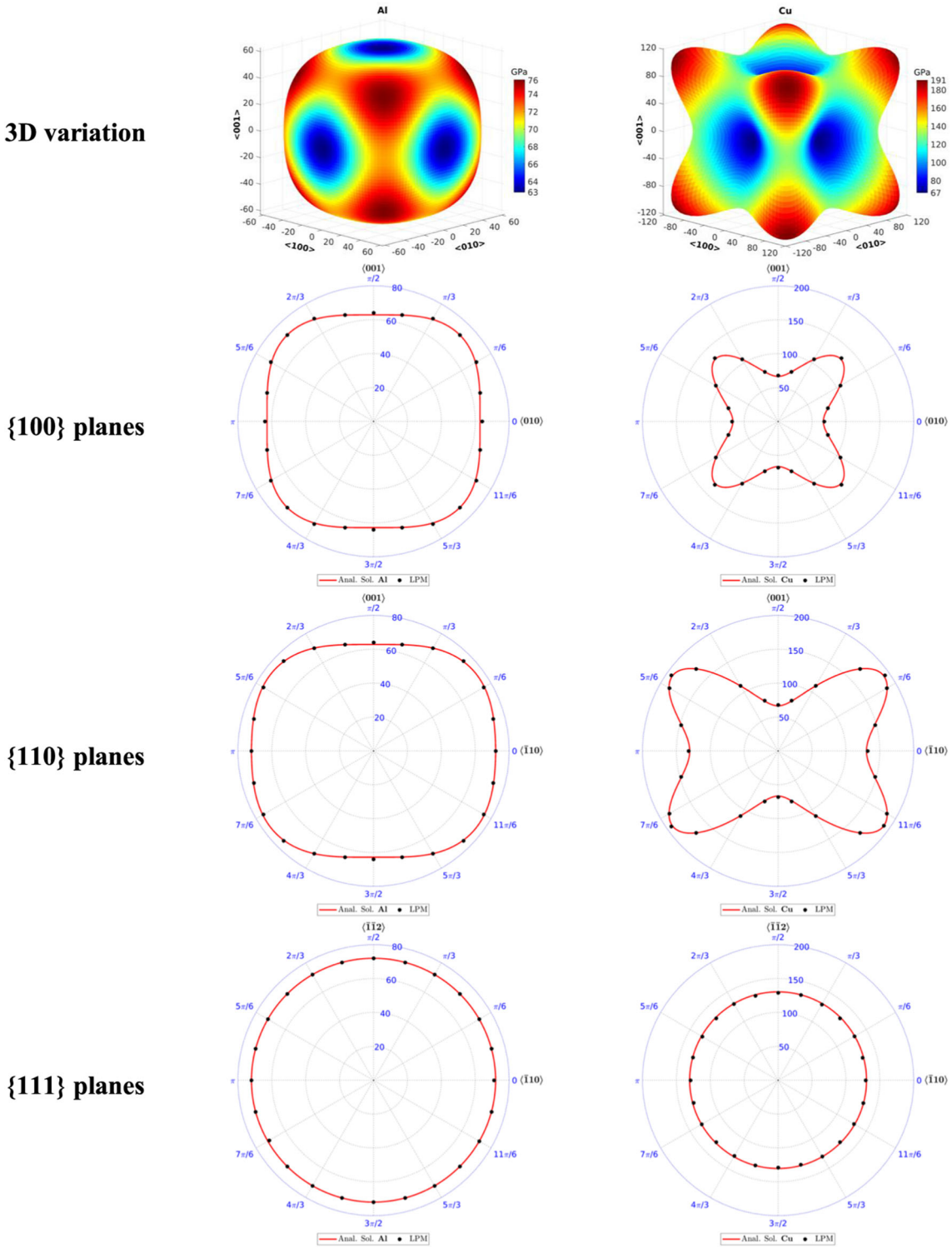

Fig. 6 Variation of Young's modulus of fcc Al and Cu single crystals

sign, therefore only the RSS in one direction is presented. The slip planes and slip directions correspond to the slip system numbers indicated in Tables 4 and 5 are given in the Appendix. The RSS by LPM is calculated using Eqs. (11) and (28). The relative error is computed as

$$Error = \frac{\left|\tau_{RSS}^{LPM} - \tau_{RSS}^{Schmid}\right|}{\left|\tau_{RSS}^{Schmid}\right|}. \tag{29}$$

It also should be noted that the predicted RSS is the average of all the material particles of the discretization. Since the calculation of RSS, both using LPM and Schmid's law, does not depend on the crystal deformation under force loading for a specific lattice (see Eq. (26) for the case of using Schmid's law), only the results of α-Fe for bcc and Al for fcc are presented. The dash lines in the Error column indicate values are not available due to the Schmid solutions are zeros.

It is clear from the comparisons presented in Tables 4 and 5, LPM can predict the RSS at high accuracy compared

Table 4 RSS comparison of bcc α-Fe under 1 MPa uniaxial tension in sample Z-direction

slip sys. #	$(0^0, 0^0, 0^0)$			$(0^0, 45^0, 0^0)$		
	τ_{RSS}^{Schmid}	τ_{RSS}^{LPM}	Error	τ_{RSS}^{Schmid}	τ_{RSS}^{LPM}	Error
1	0.0000	1.08E−12	–	0.4082	0.4017	0.0162
3	0.0000	1.19E−12	–	0.0000	2.80E−08	–
5	0.0000	− 2.97E−13	–	− 0.4082	− 0.4017	0.0162
7	0.0000	8.48E−14	–	0.0000	2.80E−08	–
9	0.4082	0.4048	0.0085	0.4082	0.4017	0.0162
11	− 0.4082	− 0.4048	0.0085	0.0000	2.65E−08	–
13	− 0.4082	− 0.4048	0.0085	− 0.4082	− 0.4017	0.0162
15	− 0.4082	− 0.4048	0.0085	0.0000	2.65E−08	–
17	0.4082	0.4048	0.0085	0.0000	1.50E−09	–
19	− 0.4082	− 0.4048	0.0085	0.0000	− 1.50E−09	–
21	− 0.4082	− 0.4048	0.0085	0.0000	− 1.50E−09	–
23	− 0.4082	− 0.4048	0.0085	0.0000	− 1.50E−09	–
25	0.2357	0.2337	0.0085	0.4714	0.4638	0.0162
27	− 0.2357	− 0.2337	0.0085	0.0000	3.15E−08	–
29	− 0.2357	− 0.2337	0.0085	0.0000	3.15E−08	–
31	0.2357	0.2337	0.0085	0.0000	1.70E−08	–
33	− 0.2357	− 0.2337	0.0085	0.2357	0.2319	0.0162
35	− 0.4714	− 0.4674	0.0085	0.0000	1.44E−08	–
37	− 0.4714	− 0.4674	0.0085	− 0.2357	− 0.2319	0.0162
39	0.4714	0.4674	0.0085	0.2357	0.2319	0.0162
41	0.2357	0.2337	0.0085	− 0.2357	− 0.2319	0.0162
43	− 0.2357	− 0.2337	0.0085	0.0000	− 1.70E−08	–
45	0.4714	0.4674	0.0085	0.0000	− 1.44E−08	–
47	0.2357	0.2337	0.0085	0.4714	0.4638	0.0162

Table 5 RSS comparison of fcc Al under 1 MPa uniaxial tension in sample Z-direction

slip sys. #	$(0^0, 0^0, 0^0)$			$(0^0, 45^0, 0^0)$		
	τ_{RSS}^{Schmid}	τ_{RSS}^{LPM}	Error	τ_{RSS}^{Schmid}	τ_{RSS}^{LPM}	Error
1	0.0000	− 1.15E−09	–	− 0.4082	− 0.3993	0.0220
3	0.4082	0.4045	0.0092	0.4082	0.3993	0.0220
5	− 0.4082	− 0.4045	0.0092	0.0000	− 5.85E−10	–
7	0.4082	0.4045	0.0092	0.4082	0.3993	0.0220
9	0.0000	1.91E−09	–	− 0.4082	− 0.3993	0.0220
11	− 0.4082	− 0.4045	0.0092	0.0000	2.76E−10	–
13	0.4082	0.4045	0.0092	0.0000	− 9.90E−07	–
15	− 0.4082	− 0.4045	0.0092	0.0000	1.65E−07	–
17	0.0000	− 1.15E−09	–	0.0000	8.25E−07	–
19	0.0000	1.91E−09	–	0.0000	9.90E−07	–
21	0.4082	0.4045	0.0092	0.0000	− 8.25E−07	–
23	− 0.4082	− 0.4045	0.0092	0.0000	− 1.65E−07	–

to the values given by Schmid's law, with the relative error within 0.92% and 2.2% for crystallographic orientation of $(0^0, 0^0, 0^0)$ and $(0^0, 45^0, 0^0)$, respectively, for both bcc and fcc lattices. The main source for this slight discrepancy is the "skin effect" inherently presented in LPM. The LPM model parameters are derived for a material particle with full neighbors, i.e., away from the boundary surfaces. Therefore, direct use of the model parameters for material particles do not have full neighbors, i.e., close to the boundary surfaces, will results in prediction inaccuracy. The smaller number of neighbors a material particle has, the worse the result of that material particle will be. It is also observed that the errors for different slip systems of the same crystallographic orientation are the same. This is because all the resolved shear stress of different slip systems are calculated based on the same stress using Eq. (28). The distributions of the stress component σ_{ZZ} are shown in Figss. 7 and 8 for bcc and fcc lattices, respectively.

As can be seen in Fig. 7, the distribution of the stress component σ_{ZZ} deviates from the analytical solution of uniform distribution of 1 MPa at material particles close to the faces for both crystallographic orientations. However, after removing a material layer of 1 mm from all the six faces, the results significantly improved (see the second column figures). The same phenomenon can be observed for the fcc Al crystal, presented in Fig. 8. Prediction significantly improved after removing material particles without full neighbors.

Similar skin effect exists in other nonlocal methods, such as peridynamics [41]. Numerous approaches have been proposed to alleviate this skin effect, such as, by using additional fictitious layer of material particles at the free surface and alternating the values of model parameters for material particles close to the surface [42]. It is not the intend of this work to illustrate application of those ideas to reduce the skin effect in LPM. To conclude, LPM can model the elastic behavior of single cubic crystals with high accuracy, compared to analytical solutions.

5 Conclusion

A novel nonlocal lattice particle method (LPM) is proposed to model the elastic behavior of cubic crystalline materials. In this paper, focus was placed on the formulation and verification of the proposed model for single crystal cases. Based on the energy equivalency between LPM and its continuum mechanics counterpart and the theory of hyper-elasticity, the model parameters were derived for cubic linear elasticity for discretizations based on the body-centered cubic lattice and face-centered cubic lattice. Different from the transformation of axes used in the classical continuum mechanics, lattice or axes rotation was employed in LPM to represent crystallographic orientation of a crystal. The validity and prediction accuracy of the proposed model

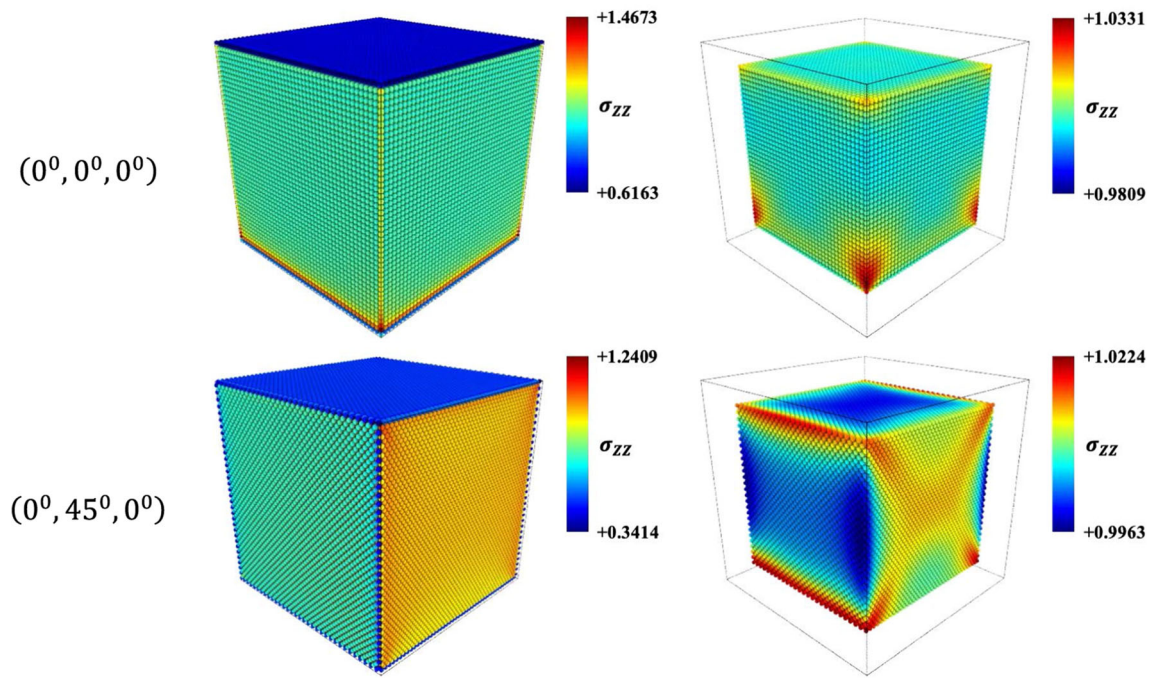

Fig. 7 Distributions of the stress component σ_{ZZ} for bcc α-Fe

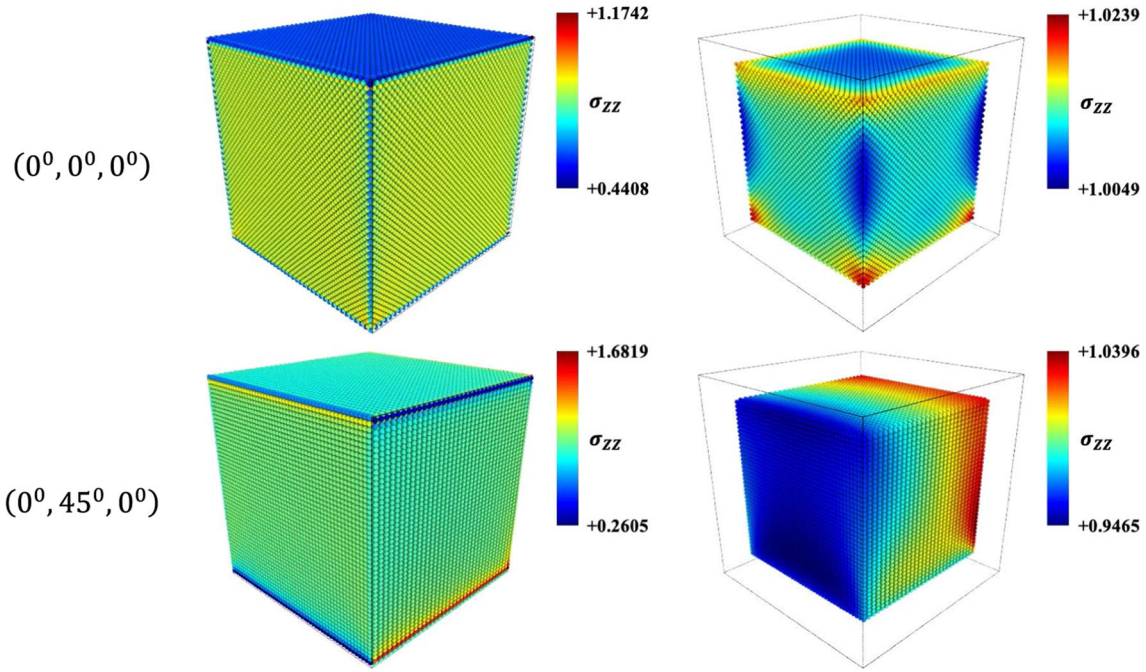

Fig. 8 Distributions of the stress component σ_{ZZ} for fcc Al

were established using two benchmark problems concerning the variation of directional Young's modulus on three crystal planes and the resolved shear stress of all slip systems of both body-centered cubic and face-centered cubic lattices.

For face-centered cubic crystals, when the anisotropy factor is greater than two, the local parameter for the second nearest neighbors becomes negative. However, this negative local parameter will not affect the performance of the model thanks to the nonlocal dependency of a bond force. This also has been demonstrated in the numerical examples using Copper crystal whose anisotropy factor is 3.2043.

Due to the assumption of full neighbors for a material particle in the derivation of the model parameters, skin effect inherently exists in LPM when directly applying those derived model parameters for material particles that do not have full neighbors. This will affect the prediction accuracy to certain degree. However, increasing discretization density and introducing a fictitious material particle layer at the boundaries like those techniques used in peridynamics can mitigate the skin effect and improve the prediction accuracy.

For computational cost of the proposed method, due to the introduction of interaction nonlocality, it inevitably increases the computational time compared to any local methods, such as the finite element method. Also, the proposed method has linear convergence rate since constant strain is assumed within a bond connecting two material particles. This will also affect the computational performance of the proposed method, since a larger number of material particles is needed for the same converged solution when compared to the finite element method where higher-order elements could be used to improve the prediction accuracy while using a smaller number of elements. However, compared to other nonlocal methods, such as peridynamics where a finite horizon is used to introduce nonlocality, the computational cost due to the employment of both the first and the second nearest neighbors is minimum. In peridynamics, a practical horizon size is at least three times of the spacing between two material particles. For regular discretization, this will include at least the neighbors to the third nearest neighbors. We will further investigate the computational cost of the proposed method for system of large number of crystals.

Future work is to apply the proposed formulation to model cubic polycrystalline materials and study the grain boundary effect on the failure behavior.

Appendix. Slip systems in fcc and bcc single crystals

See Tables 6 and 7.

Table 6 Slip systems for fcc crystals with both positive and negative slip directions [43]

slip sys. #	$\boldsymbol{m}$	$\boldsymbol{n}$	slip sys. #	$\boldsymbol{m}$	$\boldsymbol{n}$
1, 2	$\left(\frac{1}{\sqrt{2}}, \frac{-1}{\sqrt{2}}, 0\right), \left(\frac{-1}{\sqrt{2}}, \frac{1}{\sqrt{2}}, 0\right)$	$\left(\frac{1}{\sqrt{3}}, \frac{1}{\sqrt{3}}, \frac{1}{\sqrt{3}}\right)$	13, 14	$\left(\frac{-1}{\sqrt{2}}, 0, \frac{1}{\sqrt{2}}\right), \left(\frac{1}{\sqrt{2}}, 0, \frac{-1}{\sqrt{2}}\right)$	$\left(\frac{1}{\sqrt{3}}, \frac{-1}{\sqrt{3}}, \frac{1}{\sqrt{3}}\right)$
3, 4	$\left(\frac{-1}{\sqrt{2}}, 0, \frac{1}{\sqrt{2}}\right), \left(\frac{1}{\sqrt{2}}, 0, \frac{-1}{\sqrt{2}}\right)$		15, 16	$\left(0, \frac{-1}{\sqrt{2}}, \frac{-1}{\sqrt{2}}\right), \left(0, \frac{1}{\sqrt{2}}, \frac{1}{\sqrt{2}}\right)$	
5, 6	$\left(0, \frac{1}{\sqrt{2}}, \frac{-1}{\sqrt{2}}\right), \left(0, \frac{-1}{\sqrt{2}}, \frac{1}{\sqrt{2}}\right)$		17, 18	$\left(\frac{1}{\sqrt{2}}, \frac{1}{\sqrt{2}}, 0\right), \left(\frac{-1}{\sqrt{2}}, \frac{-1}{\sqrt{2}}, 0\right)$	
7, 8	$\left(\frac{1}{\sqrt{2}}, 0, \frac{1}{\sqrt{2}}\right), \left(\frac{-1}{\sqrt{2}}, 0, \frac{-1}{\sqrt{2}}\right)$	$\left(\frac{-1}{\sqrt{3}}, \frac{1}{\sqrt{3}}, \frac{1}{\sqrt{3}}\right)$	19, 20	$\left(\frac{-1}{\sqrt{2}}, \frac{1}{\sqrt{2}}, 0\right), \left(\frac{1}{\sqrt{2}}, \frac{-1}{\sqrt{2}}, 0\right)$	$\left(\frac{-1}{\sqrt{3}}, \frac{-1}{\sqrt{3}}, \frac{1}{\sqrt{3}}\right)$
9, 10	$\left(\frac{-1}{\sqrt{2}}, \frac{-1}{\sqrt{2}}, 0\right), \left(\frac{1}{\sqrt{2}}, \frac{1}{\sqrt{2}}, 0\right)$		21, 22	$\left(\frac{-1}{\sqrt{2}}, 0, \frac{1}{\sqrt{2}}\right), \left(\frac{1}{\sqrt{2}}, 0, \frac{-1}{\sqrt{2}}\right)$	
11, 12	$\left(0, \frac{1}{\sqrt{2}}, \frac{-1}{\sqrt{2}}\right), \left(0, \frac{-1}{\sqrt{2}}, \frac{1}{\sqrt{2}}\right)$		23, 24	$\left(0, \frac{-1}{\sqrt{2}}, \frac{-1}{\sqrt{2}}\right), \left(0, \frac{1}{\sqrt{2}}, \frac{1}{\sqrt{2}}\right)$	

Table 7 Slip systems for bcc crystals with both positive and negative slip directions [44]

slip sys. #	$\boldsymbol{m}$	$\boldsymbol{n}$	slip sys. #	$\boldsymbol{m}$	$\boldsymbol{n}$
1, 2	$\left(\frac{-1}{\sqrt{3}}, \frac{1}{\sqrt{3}}, \frac{1}{\sqrt{3}}\right), \left(\frac{1}{\sqrt{3}}, \frac{-1}{\sqrt{3}}, \frac{-1}{\sqrt{3}}\right)$	$\left(\frac{1}{\sqrt{2}}, \frac{1}{\sqrt{2}}, 0\right)$	25, 26	$\left(\frac{-1}{\sqrt{3}}, \frac{1}{\sqrt{3}}, \frac{1}{\sqrt{3}}\right), \left(\frac{1}{\sqrt{3}}, \frac{-1}{\sqrt{3}}, \frac{-1}{\sqrt{3}}\right)$	$\left(\frac{2}{\sqrt{6}}, \frac{1}{\sqrt{6}}, \frac{1}{\sqrt{6}}\right)$
3, 4	$\left(\frac{1}{\sqrt{3}}, \frac{-1}{\sqrt{3}}, \frac{1}{\sqrt{3}}\right), \left(\frac{-1}{\sqrt{3}}, \frac{1}{\sqrt{3}}, \frac{-1}{\sqrt{3}}\right)$		27, 28	$\left(\frac{1}{\sqrt{3}}, \frac{-1}{\sqrt{3}}, \frac{1}{\sqrt{3}}\right), \left(\frac{-1}{\sqrt{3}}, \frac{1}{\sqrt{3}}, \frac{-1}{\sqrt{3}}\right)$	$\left(\frac{2}{\sqrt{6}}, \frac{1}{\sqrt{6}}, \frac{-1}{\sqrt{6}}\right)$
5, 6	$\left(\frac{1}{\sqrt{3}}, \frac{1}{\sqrt{3}}, \frac{1}{\sqrt{3}}\right), \left(\frac{-1}{\sqrt{3}}, \frac{-1}{\sqrt{3}}, \frac{-1}{\sqrt{3}}\right)$	$\left(\frac{1}{\sqrt{2}}, \frac{-1}{\sqrt{2}}, 0\right)$	29, 30	$\left(\frac{1}{\sqrt{3}}, \frac{1}{\sqrt{3}}, \frac{-1}{\sqrt{3}}\right), \left(\frac{-1}{\sqrt{3}}, \frac{-1}{\sqrt{3}}, \frac{1}{\sqrt{3}}\right)$	$\left(\frac{2}{\sqrt{6}}, \frac{-1}{\sqrt{6}}, \frac{1}{\sqrt{6}}\right)$
7, 8	$\left(\frac{1}{\sqrt{3}}, \frac{1}{\sqrt{3}}, \frac{-1}{\sqrt{3}}\right), \left(\frac{-1}{\sqrt{3}}, \frac{-1}{\sqrt{3}}, \frac{1}{\sqrt{3}}\right)$		31, 32	$\left(\frac{1}{\sqrt{3}}, \frac{-1}{\sqrt{3}}, \frac{1}{\sqrt{3}}\right), \left(\frac{-1}{\sqrt{3}}, \frac{1}{\sqrt{3}}, \frac{-1}{\sqrt{3}}\right)$	$\left(\frac{1}{\sqrt{6}}, \frac{2}{\sqrt{6}}, \frac{1}{\sqrt{6}}\right)$
9, 10	$\left(\frac{-1}{\sqrt{3}}, \frac{1}{\sqrt{3}}, \frac{1}{\sqrt{3}}\right), \left(\frac{1}{\sqrt{3}}, \frac{-1}{\sqrt{3}}, \frac{-1}{\sqrt{3}}\right)$	$\left(\frac{1}{\sqrt{2}}, 0, \frac{1}{\sqrt{2}}\right)$	33, 34	$\left(\frac{-1}{\sqrt{3}}, \frac{1}{\sqrt{3}}, \frac{1}{\sqrt{3}}\right), \left(\frac{1}{\sqrt{3}}, \frac{-1}{\sqrt{3}}, \frac{-1}{\sqrt{3}}\right)$	$\left(\frac{1}{\sqrt{6}}, \frac{2}{\sqrt{6}}, \frac{-1}{\sqrt{6}}\right)$
11, 12	$\left(\frac{1}{\sqrt{3}}, \frac{1}{\sqrt{3}}, \frac{-1}{\sqrt{3}}\right), \left(\frac{-1}{\sqrt{3}}, \frac{-1}{\sqrt{3}}, \frac{1}{\sqrt{3}}\right)$		35, 36	$\left(\frac{1}{\sqrt{3}}, \frac{1}{\sqrt{3}}, \frac{-1}{\sqrt{3}}\right), \left(\frac{-1}{\sqrt{3}}, \frac{-1}{\sqrt{3}}, \frac{1}{\sqrt{3}}\right)$	$\left(\frac{1}{\sqrt{6}}, \frac{1}{\sqrt{6}}, \frac{2}{\sqrt{6}}\right)$
13, 14	$\left(\frac{1}{\sqrt{3}}, \frac{1}{\sqrt{3}}, \frac{1}{\sqrt{3}}\right), \left(\frac{-1}{\sqrt{3}}, \frac{-1}{\sqrt{3}}, \frac{-1}{\sqrt{3}}\right)$	$\left(\frac{1}{\sqrt{2}}, 0, \frac{-1}{\sqrt{2}}\right)$	37, 38	$\left(\frac{1}{\sqrt{3}}, \frac{1}{\sqrt{3}}, \frac{1}{\sqrt{3}}\right), \left(\frac{-1}{\sqrt{3}}, \frac{-1}{\sqrt{3}}, \frac{-1}{\sqrt{3}}\right)$	$\left(\frac{1}{\sqrt{6}}, \frac{1}{\sqrt{6}}, \frac{-2}{\sqrt{6}}\right)$
15, 16	$\left(\frac{1}{\sqrt{3}}, \frac{-1}{\sqrt{3}}, \frac{1}{\sqrt{3}}\right), \left(\frac{-1}{\sqrt{3}}, \frac{1}{\sqrt{3}}, \frac{-1}{\sqrt{3}}\right)$		39, 40	$\left(\frac{-1}{\sqrt{3}}, \frac{1}{\sqrt{3}}, \frac{1}{\sqrt{3}}\right), \left(\frac{1}{\sqrt{3}}, \frac{-1}{\sqrt{3}}, \frac{-1}{\sqrt{3}}\right)$	$\left(\frac{1}{\sqrt{6}}, \frac{-1}{\sqrt{6}}, \frac{2}{\sqrt{6}}\right)$
17, 18	$\left(\frac{1}{\sqrt{3}}, \frac{-1}{\sqrt{3}}, \frac{1}{\sqrt{3}}\right), \left(\frac{-1}{\sqrt{3}}, \frac{1}{\sqrt{3}}, \frac{-1}{\sqrt{3}}\right)$	$\left(0, \frac{1}{\sqrt{2}}, \frac{1}{\sqrt{2}}\right)$	41, 42	$\left(\frac{1}{\sqrt{3}}, \frac{1}{\sqrt{3}}, \frac{1}{\sqrt{3}}\right), \left(\frac{-1}{\sqrt{3}}, \frac{-1}{\sqrt{3}}, \frac{-1}{\sqrt{3}}\right)$	$\left(\frac{1}{\sqrt{6}}, \frac{-2}{\sqrt{6}}, \frac{1}{\sqrt{6}}\right)$
19, 20	$\left(\frac{1}{\sqrt{3}}, \frac{1}{\sqrt{3}}, \frac{-1}{\sqrt{3}}\right), \left(\frac{-1}{\sqrt{3}}, \frac{-1}{\sqrt{3}}, \frac{1}{\sqrt{3}}\right)$		43, 44	$\left(\frac{1}{\sqrt{3}}, \frac{1}{\sqrt{3}}, \frac{-1}{\sqrt{3}}\right), \left(\frac{-1}{\sqrt{3}}, \frac{-1}{\sqrt{3}}, \frac{1}{\sqrt{3}}\right)$	$\left(\frac{-1}{\sqrt{6}}, \frac{2}{\sqrt{6}}, \frac{1}{\sqrt{6}}\right)$
21, 22	$\left(\frac{1}{\sqrt{3}}, \frac{1}{\sqrt{3}}, \frac{1}{\sqrt{3}}\right), \left(\frac{-1}{\sqrt{3}}, \frac{-1}{\sqrt{3}}, \frac{-1}{\sqrt{3}}\right)$	$\left(0, \frac{1}{\sqrt{2}}, \frac{-1}{\sqrt{2}}\right)$	45, 56	$\left(\frac{1}{\sqrt{3}}, \frac{-1}{\sqrt{3}}, \frac{1}{\sqrt{3}}\right), \left(\frac{-1}{\sqrt{3}}, \frac{1}{\sqrt{3}}, \frac{-1}{\sqrt{3}}\right)$	$\left(\frac{-1}{\sqrt{6}}, \frac{1}{\sqrt{6}}, \frac{2}{\sqrt{6}}\right)$
23, 24	$\left(\frac{-1}{\sqrt{3}}, \frac{1}{\sqrt{3}}, \frac{1}{\sqrt{3}}\right), \left(\frac{1}{\sqrt{3}}, \frac{-1}{\sqrt{3}}, \frac{-1}{\sqrt{3}}\right)$		47, 48	$\left(\frac{1}{\sqrt{3}}, \frac{1}{\sqrt{3}}, \frac{1}{\sqrt{3}}\right), \left(\frac{-1}{\sqrt{3}}, \frac{-1}{\sqrt{3}}, \frac{-1}{\sqrt{3}}\right)$	$\left(\frac{-2}{\sqrt{6}}, \frac{1}{\sqrt{6}}, \frac{1}{\sqrt{6}}\right)$

References

1. Mahfoz-Kotb H, Salaün AC, Mohammed-Brahim T, Le Bihan F, El-Marssi M (2003) Polycrystalline silicon thin films for MEMS applications. In: Thin Solid Films, Elsevier, pp. 422–426. https://doi.org/10.1016/S0040-6090(02)01201-4
2. Adams BL, Olson T (1998) The mesostructure - Properties linkage in polycrystals. Prog Mater Sci 43:1–87. https://doi.org/10.1016/s0079-6425(98)00002-4
3. Corigliano A, Ghisi A, Langfelder G, Longoni A, Zaraga F, Merassi A (2011) A microsystem for the fracture characterization of polysilicon at the micro-scale. Eur J Mech A/Solids 30:127–136. https://doi.org/10.1016/j.euromechsol.2010.09.006
4. Abdolvand H, Wright J, Wilkinson AJ (2018) Strong grain neighbour effects in polycrystals. Nat Commun. https://doi.org/10.1038/s41467-017-02213-9
5. Benedetti I, Barbe F (2013) Modelling polycrystalline materials: an overview of three-dimensional grain-scale mechanical models. J Multiscale Model 5:1350002. https://doi.org/10.1142/S1756973713500029
6. Lee CC, Huang PC (2019) Overview of computational modeling in nano/micro scaled thin films mechanical properties and its applications. C Comput Model Eng Sci 120:239–260. https://doi.org/10.32604/cmes.2019.06859
7. Shenderova OA, Brenner DW, Omeltchenko A, Su X, Yang LH (2000) Atomistic modeling of the fracture of polycrystalline diamond. Phys Rev B 61:3877–3888. https://doi.org/10.1103/PhysRevB.61.3877
8. Zhao Y, Xu Y, Liu X, Zhu J, Luo S-N (2019) Grain size effects on dynamic fracture instability in polycrystalline graphene under tear loading. J Mater Res 34:2209–2217. https://doi.org/10.1557/jmr.2019.76
9. Simonovski I, Cizelj L (2013) Cohesive element approach to grain level modelling of intergranular cracking. Eng Fract Mech 110:364–377. https://doi.org/10.1016/j.engfracmech.2013.05.011
10. Lin L, Wang X, Zeng X (2017) The role of cohesive zone properties on intergranular to transgranular fracture transition in polycrystalline solids. Int J Damage Mech 26:379–394. https://doi.org/10.1177/1056789515618732
11. Lu M, Wang F, Zeng X, Chen W, Zhang J (2020) Cohesive zone modeling for crack propagation in polycrystalline NiTi alloys using molecular dynamics. Theor Appl Fract Mech 105:102402. https://doi.org/10.1016/j.tafmec.2019.102402
12. Sukumar N, Srolovitz DJ, Baker TJ, Prévost JH (2003) Brittle fracture in polycrystalline microstructures with the extended finite

element method. Int J Numer Methods Eng 56:2015–2037. https://doi.org/10.1002/nme.653
13. Beese S, Loehnert S, Wriggers P (2018) 3D ductile crack propagation within a polycrystalline microstructure using XFEM. Comput Mech 61:71–88. https://doi.org/10.1007/s00466-017-1427-y
14. Clayton JD, Knap J (2015) Phase field modeling of directional fracture in anisotropic polycrystals. Comput Mater Sci 98:158–169. https://doi.org/10.1016/j.commatsci.2014.11.009
15. Clayton JD, Knap J (2016) Phase field modeling and simulation of coupled fracture and twinning in single crystals and polycrystals. Comput Methods Appl Mech Eng 312:447–467. https://doi.org/10.1016/j.cma.2016.01.023
16. Clayton JD (2019) Computational modeling of dual-phase ceramics with finsler-geometric phase field mechanics. C Comput Model Eng Sci 120:333–350. https://doi.org/10.32604/cmes.2019.06342
17. Jivkov AP, Stevens NPC, Marrow TJ (2006) A three-dimensional computational model for intergranular cracking. Comput Mater Sci 38:442–453. https://doi.org/10.1016/j.commatsci.2006.03.012
18. Jivkov AP, Stevens NPC, Marrow TJ (2008) Mesoscale mechanical model for intergranular stress corrosion cracking and implications for microstructure engineering. J Press Vessel Technol. https://doi.org/10.1115/1.2937736
19. Zhu N, De Meo D, Oterkus E (2016) Modelling of granular fracture in polycrystalline materials using ordinary state-based peridynamics. Materials (Basel). https://doi.org/10.3390/ma9120977
20. Gur S, Sadat MR, Frantziskonis GN, Bringuier S, Zhang L, Muralidharan K (2019) The effect of grain-size on fracture of polycrystalline silicon carbide: A multiscale analysis using a molecular dynamics-peridynamics framework. Comput Mater Sci 159:341–348. https://doi.org/10.1016/j.commatsci.2018.12.038
21. Li M, Lu W, Oterkus E, Oterkus S (2020) Thermally-induced fracture analysis of polycrystalline materials by using peridynamics. Eng Anal Bound Elem 117:167–187. https://doi.org/10.1016/j.enganabound.2020.04.016
22. Tadmor EB, Ortiz M, Phillips R (1996) Quasicontinuum analysis of defects in solids. Philos Mag A 73:1529–1563
23. Kochmann DM, Amelang JS (2016) The quasicontinuum method: theory and applications. In: W. C., T. G. (Eds.), Multiscale Mater. Model. Nanomechanics, Springer, Cham, pp. 159–193. https://doi.org/10.1007/978-3-319-33480-6_5
24. Yang S, Chen Y (2015) Concurrent atomistic and continuum simulation of bi-crystal strontium titanate with tilt grain boundary. Proc R Soc A Math Phys Eng Sci 471:20140758. https://doi.org/10.1098/rspa.2014.0758
25. Chen Y, Shabanov S, McDowell DL (2019) Concurrent atomistic-continuum modeling of crystalline materials. J Appl Phys 126:101101. https://doi.org/10.1063/1.5099653
26. Chung DH, Buessem WR (1967) The Elastic Anisotropy of Crystals. J Appl Phys 38:2010–2012. https://doi.org/10.1063/1.1709819
27. Krasovskii AY, Vainshtok VA (1977) Crystallography of cleavage in BCC metals. Strength Mater 9:1091–1099. https://doi.org/10.1007/BF01528588
28. Weinberger CR, Boyce BL, Battaile CC (2013) Slip planes in bcc transition metals. Int Mater Rev 58:296–314. https://doi.org/10.1179/1743280412Y.0000000015
29. Chen H, Lin E, Jiao Y, Liu Y (2014) A generalized 2D non-local lattice spring model for fracture simulation. Comput Mech 54:1541–1558. https://doi.org/10.1007/s00466-014-1075-4
30. Chen H, Liu Y (2016) A non-local 3D lattice particle framework for elastic solids. Int J Solids Struct 81:411–420. https://doi.org/10.1016/j.ijsolstr.2015.12.026
31. Chen H, Jiao Y, Liu Y (2016) A nonlocal lattice particle model for fracture simulation of anisotropic materials. Compos Part B Eng 90:141–151. https://doi.org/10.1016/j.compositesb.2015.12.028
32. Chen H, Lin E, Liu Y (2014) A novel Volume-Compensated Particle method for 2D elasticity and plasticity analysis. Int J Solids Struct 51:1819–1833. https://doi.org/10.1016/j.ijsolstr.2014.01.025
33. Ostoja-Starzewski M (2002) Lattice models in micromechanics. Appl Mech Rev 55:35–60. https://doi.org/10.1115/1.1432990
34. Chen H (2019) Constructing continuum-like measures based on a nonlocal lattice particle model: Deformation gradient, strain and stress tensors. Int J Solids Struct 169:177–186. https://doi.org/10.1016/j.ijsolstr.2019.04.014
35. Lin E, Chen H, Liu Y (2015) Finite element implementation of a non-local particle method for elasticity and fracture analysis. Finite Elem Anal Des 93:1–11. https://doi.org/10.1016/j.finel.2014.08.008
36. Bunge H-J (1969) Texture Analysis in Materials Science: Mathematical Methods. Butterworth-Heinemann. https://doi.org/10.1016/C2013-0-11769-2
37. Lubarda VA (1997) New estimates of the third-order elastic constants for isotropic aggregates of cubic crystals. J Mech Phys Solids 45:471–490. https://doi.org/10.1016/S0022-5096(96)00113-5
38. Courtney TH (2005) Mechanical Behavior of Materials, 2nd ed., Waveland Press, Inc.
39. Schmid E, Boas W (1968) Plasticity of Crystals: with special Reference to Metals. Chapman and Hall, London
40. Huang Y (1991) A user-material subroutine incroporating single crystal plasticity in the ABAQUS finite element program, Report MECH-178, Cambridge, MA
41. Bobaru F, Foster JT, Geubelle PH, Silling SA (2016) Handbook of Peridynamic Modeling. CRC Press, Boca Raton
42. Hu Y, Chen H, Spencer BW, Madenci E (2018) Thermomechanical peridynamic analysis with irregular non-uniform domain discretization. Eng Fract Mech 197:92–113. https://doi.org/10.1016/j.engfracmech.2018.02.006
43. Kalidindi SR (1992) Polycrystal plasticity: Constitutive modeling and deformation processing, Massachusetts Institute of Technology
44. Akpama HK, Ben Bettaieb M, Abed-Meraim F (2016) Numerical integration of rate-independent BCC single crystal plasticity models: comparative study of two classes of numerical algorithms. Int J Numer Methods Eng 108:363–422. https://doi.org/10.1002/nme.5215